Comparison of fluorine removal performance and mechanism of spheroidal magnesium oxide before and after lanthanum modification

Qiang Zhang
Southeastern University
Yuming Zhou (ymzhchem@163.com)
Southeast University
Qingzhao Yao
Southeast University
Fanli Zhang
Southeast University
Wanying Chen
Southeast University
Yang Liu
Varun Water Environmental Technology Co

Research Article

Keywords: spheroidal magnesium oxide, lanthanum modified, defluorination mechanism, fluorine removal performance, adsorption kinetics, adsorption thermodynamics

Posted Date: March 22nd, 2022

DOI: https://doi.org/10.21203/rs.3.rs-1409919/v1

Abstract

Use simple magnesium salt as raw material, the magnesium oxide precursor powder was synthesized, and then the spheroidal magnesium oxide (SMO) was synthesized by controlled temperature calcination. Then lanthanum-modified spheroidal magnesium oxide (LSMO) was prepared by impregnation. The SMO and LSMO were characterized by X-ray diffraction (XRD), field emission scanning electron microscopy (SEM), N_2 adsorption-desorption, infrared spectroscopy (FT-IR) and X-ray photoelectron spectroscopy (XPS). For the initial fluorine concentration of 10mg/L fluoride solution, the maximum fluoride removal efficiency of 15% impregnation ratio lanthanum modified spheroidal magnesium oxide (15LSMO) is 93.1%, which is higher than 82.7% of SMO, far lower than the international standard 1.5mg/L. In addition, in the pH range of 2-11, and in the presence of interfering ions, the effect of 15LSMO also meets the international standards for fluoride removal. For the enhancement of fluoride removal effect of defluoridation agent, lanthanum modified material defluoridation mechanism changes have profound insights.

1. Introduction

In the past decades, due to the excessive use of earth resources by human beings, fluoride ions infiltrated into groundwater caused by mineral exploitation, or fluoride wastewater produced by industrial production have posed great threats to nature and human beings themselves (Nur et al. 2014). Excessive fluoride uptake by plants will lead to impaired photosynthesis and excessive fluoride intake by humans will lead to skeletal fluorosis. Therefore, fluoride pollution is generally considered to be a serious environmental health hazard in the world. The WHO has set fluoride concentrations in drinking water at less than 1.5mg/L (Ayoob and Gupta 2006), while China has set fluoride concentrations at less than 1mg/L. Subsequently, scientists carry out a large number of experimental studies on fluorine removal, and developed various methods to effectively treat various fluorine-containing wastewater, such as chemical precipitation (Turner et al. 2005), adsorption (Maliyekkal et al. 2006), ion exchange (Sairam Sundaram and Meenakshi 2009). Among them, adsorption method is the focus of fluorine removal research because of the advantages of simple operation and low cost.

The adsorption method includes carbon-based materials, natural minerals, metal materials, polymers and resins, biological materials, etc (He et al. 2020). Metal materials stand out because of their easy synthesis and high efficiency in fluorine removal, and magnesium oxide as a metal material compared with traditional activated alumina with high selectivity and high efficiency in fluorine removal, as well as reduce the harm of overflow of metal ions on the human body and become a new green adsorption material. At the nanoscale, magnesium oxide has highly concentrated structural defects, so magnesium oxide has the advantages of high porosity, large specific surface area, and a large number of hydroxyl sites (Maliyekkal et al. 2010).Of course, the excellent adsorption performance of magnesium oxide adsorbent has been widely concerned by scientists. Li et al. successfully prepared porous hollow magnesium oxide microspheres with a specific surface area of $130 m^2 \cdot g^{-1}$ and adsorption capacity of more than $120 mg \cdot g^{-1}$ by using magnesium chloride as magnesium source (Li et al. 2014). In addition,

Xavy Borgohain et al. synthesized different nano-magnesium oxide structures through different magnesium sources and different synthesis methods (Borgohain et al. 2020). Zhang et al. successfully prepared hollow spheres of magnesium oxide using magnesium sulfate heptahydrate, with an adsorption capacity greater than 182.4 mg•g^{-1} (Zhang et al. 2021). Kuang et al. used magnesium acetate and spray drying to successfully prepare spherical magnesium oxide nanostructures, and they have excellent adsorption properties for Pb(Ⅱ) and Cd(Ⅱ) (Kuang et al. 2019). The above work is sufficient to prove the excellent adsorption performance of magnesium oxide and the simple preparation process, due to the size limitation, subsequent work will be affected, so a larger size magnesium oxide adsorbent is required. In this research, we successfully synthesized a spheroidal magnesium oxide with excellent fluorine removal performance, stable physical and chemical structure and a diameter of 20–30μm.

Based on the preparation of spheroidal magnesium oxide, in order to further optimize its fluorine removal performance and meet the requirements of deep fluorine removal in specific situations, lanthanum modification on the surface of magnesium oxide has become our new goal. As a rare earth element, lanthanum has strong selectivity to fluoride ions due to its hard acidity and the hard alkalinity of fluoride (Zhang et al. 2016). In recent years, the optimization of lanthanum's fluoride removal performance has been reflected in some researches. He et al. successfully modified mesoporous alumina with lanthanum. Compared with Mesoporous alumina (MA), La/MA significantly improved the fluorine removal performance, and the adsorption capacity was about 26.45mg•g^{-1} (He et al. 2019). Shi et al. successfully prepared lanthanum modified activated alumina (LAA). Compared with AA, LAA has an adsorption capacity of 16.9mg•g^{-1} (Shi et al. 2013). However, there is no report about the removal of fluoride by lanthanum-modified magnesium oxide. The current research requires us to deepen the understanding of the design, synthesis and mechanism of fluorine adsorbents.

Based on the above research, we synthesized spheroidal magnesium oxide SMO and lanthanum-modified spheroidal magnesium oxide (LSMO). Comparing the adsorption behavior of SMO and LSMO on fluoride ions in water, the effects of time, initial fluoride ion concentration, pH, and interfering ions on the ability of fluoride removal were studied, and the adsorption mechanism was understood through adsorption kinetics and adsorption isotherms. The fluorine removal experiment found that 15LSMO (LSMO with 15% immersion ratio) had the best fluoride removal effect, so the subsequent analysis and experiment mainly used SMO and 15LSMO for comparison. Then, SMO and 15LSMO were characterized by XRD, FT-IR, BET, XPS, SEM and other characterization methods, and the mechanism of fluorine removal was discussed. These works have enriched and perfected the different interpretations of the fluorine removal performance and the fluorine removal mechanism of spheroidal magnesium oxide before and after lanthanum modification, consequently it is conducive to future research.

2. Experimental Part

2.1. Materials

All the chemicals used in this study were analytical grades, including NaF, $MgSO_4 \cdot 7H_2O$, urea, $La(NO_3)_3 \cdot 6H_2O$, HCl, NaOH, KNO_3, Na_2SO_4, Na_2CO_3, KH_2PO_4, NaCl, $NaHCO_3$, all purchased from Sinopharm Chemical Reagents Co, LTD.

2.2. Synthesis

The synthesis steps of spheroidal magnesium oxide include,10g $MgSO_4 \cdot 7H_2O$, 3g urea and 40ml water were mixed and stirred for 30min, then placed in a reaction kettle, and reacted in an oven at 100℃ for 12h. The white precipitate was centrifuged and cleaned, and then dried at 80℃. Then the white precipitate was calcined for 8h at a heating rate of 1℃/min to obtain the spheroidal magnesium oxide adsorbent (SMO).

The synthesis steps of lanthanum-modified spheroidal magnesium oxide include,1gSMO, $La(NO_3)_3 \cdot 6H_2O$ and 10mL water were mixed and stirred for 12h, the precipitation was centrifuged and cleaned, then dried in the oven, and then annealed at 400℃ for 4h, lanthanum-modified spheroidal magnesium oxide (LSMO) was obtained. LSMO with different doping amounts was obtained through different impregnation ratios (mass ratios of lanthanum nitrate and spheroidal magnesium oxide were 5%, 10%, 15%, 20%).

2.3. Characterization

The morphology and EDAS of SMO and LSMO were analyzed by scanning electron microscope (FEI, Inspect F50). SMO and LSMO were characterized by X-ray diffraction analyzer (XRD, Ultima IV). Fourier transform infrared spectrometer (FT-IR, Nicolet 5700) was used to characterize the adsorption mechanism of the materials before and after adsorption. The specific surface area and pore size of the materials were analyzed by automatic specific surface and porosity analyzer (BET, Micromeritics 2020). X-ray photoelectron spectroscopy (XPS, Thermo Kalpha) was used to analyze the surface chemical properties of the materials before and after adsorption.

2.4. Adsorption Experiments

Add 1000mL deionized water with 2.210 g NaF and configure it into 1000mg/L fluoride ion stock solution and store it in refrigerator. The raw fluoride ion solution was diluted to fluoride ion solution of different concentrations, 1g/L adsorption material was added to 10mg/L fluoride ion solution and placed in a centrifugal tube, and stirred in an isothermal (25℃) shaker at 200rpm for 180min. After standing for 1h, the supernatant was taken and the fluoride ion concentration was measured using F ion selective electrode (PF-202). The pH of fluoride ion solution was adjusted with 0.1mol/L HCl and NaOH solution, and then the above fluoride removal experiment was repeated to understand the influence of pH on the material fluoride removal. Use KNO_3, Na_2SO_4, Na_2CO_3, KH_2PO_4, NaCl, $NaHCO_3$, configuration is 100 mg/L to interference ions concentration of fluorine ion solution, in order to understand interference ions on the material in addition to the influence of fluorine. The remaining waste liquid was collected and filtered out

of the adsorbent, and dried for 12h at 100℃ for further experiments. The total adsorption quantity Q_e (mg/g) of fluoride ion is calculated by formula (1):

$$Q_{\mathrm{e}} = \frac{(C_0 - C_e)V}{m}$$

1

Fluoride removal rate (%) is calculated by Formula (2):

$$R_F = \frac{C_0 - C_e}{C_0} \times 100\%$$

2

C_0,$C_e$respectively represent the initial concentration and equilibrium concentration of F^- in solution (mg/L), V and M respectively represent the volume of solution (mL) and the mass of adsorbent (g).

In order to conduct adsorption isotherm studies, multiple initial F^- concentrations in the range of 1mg/L to 200mg/L of F^- mother liquor were used for adsorption equilibrium experiments. Other parameters were set as follows: 50mL fluoride ion solution was added with 50mg adsorbent, adsorption time was 180min, initial pH range was 7, temperature range was 25°C, stirring speed was 200rpm.

2.5. Isotherm models

In this research, two nonlinear isotherm equations (Langmuir, Freundlich) were tested and the adsorption mechanism was reasonably predicted (Yin et al. 2018, Tan et al. 2008).

Langmuir equation is shown in Formula (3):

$$q_e = \frac{q_m K_L C_e}{1 + K_L C_e}$$

3

q_e(mg/g) is the adsorption capacity, q_m(mg/g) is the saturated adsorption capacity, $C_e$is the equilibrium concentration of F^-, K_L(L/mg) is the Langmuir adsorption constant.

Freundlich equation is shown in Formula (4):

$$q_e = K_F C_e^{\frac{1}{n}}$$

4

K_F(mg·g^{-1}) ·(mg·L^{-1})$^{-1/n}$ is the binding energy constant, 1/n in Freundlich model is the heterogeneity factor (Cadaval et al. 2015).

2.6. Kinetic models

In this research, two nonlinear dynamics models (pseudo-first-order and pseudo-second-order) were tested using these nonlinear dynamics equations to analyze the adsorption rate and predict the determining steps of the adsorption rate ((1907) (Ho 2000)

The pseudo-first-order dynamics equation is shown in Formula (5):

$$q_t = q_e{}^{(1-e^{-K_1 t})}$$

5

The pseudo-second-order kinetic equation is shown in Formula (6):

$$q_t = \frac{K_2 q_e{}^2 t}{1 + K_2 q_e t}$$

6

q_e and q_t are the adsorption capacity of F^- at equilibrium and at time t (min), respectively.K_1(min^{-1}) is the pseudo-first-order adsorption rate constant, and K_2($g{\cdot}mg^{-1}{\cdot}min^{-1}$) is the pseudo-second-order adsorption rate constant.

3. Results And Discussion

3.1. Characterization

3.1.1. XRD analysis

In order to analyze the structural differences between SMO and LSMO, the samples were characterized by XRD. It can be seen from Fig. 1 that SMO has obvious diffraction peaks at 2θ = 38.1, 42.6, 62.1, 74.2 and 78.3°. According to the literature and the standard card (PDF #45–0946), the above diffraction peaks belong to the (111), (200), (220), (311) and (222) lattice planes of magnesium oxide, respectively, So the formation of magnesium oxide was confirmed (Sutradhar et al. 2011). However, in the XRD spectrum of 15LSMO, the diffraction peaks of 2θ = 38.1 and 74.2°. are not obvious, which belong to (111) and (311) crystal planes respectively This can be explained by the successful loading of lanthanum on the surface of magnesium oxide. The three main diffraction peaks of 15LSMO are well matched with SMO, and no new diffraction peaks are generated, indicating that the lanthanum oxide formed by impregnation and calcination of lanthanum nitrate is uniformly distributed on the surface of SMO.

3.1.2 Microscopic study

In order to observe the morphology of the formed SMO and LSMO, the product was characterized by SEM. According to Fig. 2(a), we found that the magnesia precursor powder was calcined to form a spheroidal oxide packaged by flake magnesia. Figure 2(b) is the scan image of 15LSMO. After loading,

there is no change in the size of the morphology. And the Fig. 2(c) and Fig. 2(d) after scanning by EDS prove that lanthanum was successfully loaded on the surface of SMO. And Fig. 2(d) is the scanning distribution diagram of 15LSMO lanthanum, which can prove that lanthanum is evenly distributed on the surface of SMO.

In order to further study the morphological characteristics of SMO, the SMO was characterized by TEM, and the characterization results are shown in Fig. 3. Figure 3(a) is a TEM image of scattered flake magnesium oxide from the assembled spherical magnesium oxide, it can be found that there are many void sites on the surface of the flaky magnesia, which are caused by the overflow of carbon dioxide and water during the calcination process. Of course, this void site provides void sites for the adsorption of fluorine and the loading of lanthanum. The inset in Fig. 3(a) is the SAED image corresponding to flaky magnesium oxide, showing that the flaky magnesium oxide has a polycrystalline and crystal structure, the crystal plane corresponds to the XRD pattern. Figure 3(b) is the edge TEM image of SMO. It can be seen that the morphology of the flake-shaped magnesium oxide matches the SEM image of Fig. 2(a).

3.1.3 BET analysis

The microstructure of SMO and 15LSMO is further analyzed by BET characterization. Figure 4 shows the N_2 adsorption and desorption isotherms of SMO and 15LSMO, and the corresponding pore size distribution curves. According to the classification of the article, the isotherm of SMO belongs to type IV, H3 type hysteresis loop, the isotherm of LSMO also belongs to type IV, H3 type hysteresis loop (Sing 1985). The hysteresis ring of type IV isotherm is its remarkable feature, which represents the condensation of the mesoporous capillary, which is a typical mesoporous adsorbent; the H3 type hysteresis ring represents the abundant fissure-type pores in it. After comparing the isotherms of a and c in Fig. 4, it is found that they belong to the same type, because most of the pores are composed of SMO, while the comparison of b and d shows that the pore peak is at the same 4nm, while d contains more pores at 17nm. The peak is formed due to the shrinkage of the gaps between the flake magnesium oxide due to the loading of lanthanum, which is consistent with the SEM observation. The detailed BET data is shown in Table 1. The specific surface area and pore diameter of 15LSMO have been improved compared to SMO, which also provides a basis for the subsequent enhancement of fluorine removal capacity.

3.1.4 FTIR analysis

In order to explain the fluorine removal mechanism of the materials, the two materials were characterized by infrared before and after the fluorine removal. The results are shown in Fig. 5. Figure 5a is the infrared spectrum of SMO before and after fluorine adsorption. The peaks at 3430cm^{-1} and 1640cm^{-1} before adsorption belong to the stretching vibration of the OH band and the bending vibration of the H-OH band formed by the adsorbed water in the air (Zhang et al. 2015). The strong peak near 3699cm^{-1} after fluorine adsorption is attributed to the A_{2u}(OH) lattice vibration caused by the formation of $Mg(OH)_2$ (Niu et al. 2006). Moreover, after adsorption, the peak intensity at 3430 cm^{-1} is greatly reduced, which proves

that the substitution of OH is part of the mechanism of fluoride ion adsorption. The peaks at 1470cm^{-1}, 1129cm^{-1} and 868cm^{-1} before adsorption belong to the antisymmetric stretching vibration peak, the symmetric stretching vibration peak and the out-of-plane bending vibration absorption peak of CO_3^{2-}, respectively (Xu and Zeng 2003). After fluorine adsorption, the disappearance of the 1129cm^{-1} peak indicates that carbonate also plays a role in replacing fluoride ions. The range of 400cm^{-1}-800cm^{-1} basically belongs to the infrared characteristics of the metal bond. The peaks at 640cm^{-1} and 438cm^{-1} before adsorption are the significant infrared characteristics of MgO. The peak at 575cm^{-1} after adsorption belongs to the tensile vibration of Mg-F (Jin et al. 2015). It is proved that the fluorine removal mechanism of magnesium oxide is the result of the combined action of hydroxyl, carbonate and metal bond adsorption.

Figure 5.b shows the infrared spectra of 15LSMO before and after fluorine adsorption. We can find that the continuous double peak at 1463cm^{-1} is the typical infrared characteristic of lanthanum carbonate (Sun et al. 2020). Compared with the one before the adsorption in Fig. 5.a,the extra peak, t 1069cm^{-1} before the adsorption in Fig. 5.b is the infrared characteristic of lanthanum carbonate, The split with the peak near 1100cm^{-1} and 1463cm^{-1} indicates the presence of non-equivalent carbonate ions, which verifies the successful loading of lanthanum on the other hand, and the peak near 1100cm-1 disappears after adsorption, which is similar to the carbonate ion in Fig. 5.a. The peak at 3697 cm^{-1} after adsorption is attributed to the A_{2u}(OH) lattice vibration caused by the formation of $Mg(OH)_2$ and $La(OH)_3$. Before adsorption, 418cm^{-1} is the infrared characteristic of MgO, while the peaks near 609cm^{-1} belong to the infrared characteristics of MgO and La_2O_3 (Chowdhury et al. 2016, Khalil et al. 2021), while the peak at 455cm^{-1} after adsorption is the infrared characteristic of MgO covered with F, and the peak at 566cm^{-1} is the formation of the bond between metal and F (Mg-F and La-F). In summary, it can be found that the fluorine removal mechanism of SMO and 15LSMO is basically similar.

3.1.5 XPS analysis

In order to further study the fluorine removal mechanism of the material, XPS characterization was performed on the material before and after fluorine adsorption. Figure 6 and Fig. 7 are the relevant XPS spectra of SMO and 15LSMO, respectively. From Fig. 5.a and Fig. 6.a, we can find that a new peak of 684.9eV belonging to F1s appears after adsorption, which clearly proves the effective adsorption of fluorine by the material (Sugama et al. 1998). Figure 6.b and Fig. 7.b are the C1s spectra before and after the adsorption of SMO and 15LSMO, the peak values are 284.8 eV (after calibration) and 289.6 eV, 284.8 eV and 289.6 eV are organic carbon and carbonate, respectively peak (Jia et al. 2013). Carbonate is the thermal decomposition of urea in the raw material and the supply of air atmosphere. After adsorption, the peak of carbonate is reduced to a certain extent, which means that carbonate is consumed in fluorine adsorption. Figure 6.c and Fig. 7.c are the O1s spectra before and after the adsorption of SMO and 15LSMO, with a total of 529.7 eV, 531.5 eV, 532.3 eV and 533.5 eV peaks. 529.7 eV belongs to the lattice oxygen atom combined with metal (Wuttke et al. 2008). The peaks at 531.5 and 533.5 eV belong to the metal hydroxide and the hydroxyl group of adsorbed water, respectively (Benedetti et al. 2011, Newberg et

al. 2011). The peak at 532.3 eV is due to the presence of oxygen in carbonate (Descostes et al. 2000, Wang et al. 2017). In Fig. 6.c and Fig. 7.c, we can find that the metal-bound lattice oxygen atoms are transformed into metal hydroxides and hydroxyl groups of adsorbed water after adsorption, which is consistent with the results of the FT-IR spectrum. The peak of the oxygen atom in the carbonate is also reduced, which is consistent with the C1s spectrum. In Fig. 7.c, the hydroxyl groups that have adsorbed water before adsorption may be caused by the lanthanum impregnation process. Figure 6.d and Fig. 7.d are the F1s spectra of SMO and 15LSMO after adsorption, of which 684.8, 686.5 and 689.4eV belong to metal complex MF, metal hydroxide fluoride M-FOH and metal fluoride cover, respectively (Wang et al. 2017, Li et al. 2016). Figure 6.e and Fig. 7.e are the Mg2p spectra before and after the adsorption of SMO and 15LSMO. Both have peaks near 49.1eV and 50.4eV before adsorption, of which 49.1eV is the Mg-OH peak, and near 50.3eV is Mg-O Peak (Wuttke et al. 2008, Li et al. 2014). After adsorption, the position of the peak shifts to the left, and the binding energy increases. This is due to the adsorption of fluorine, and the Mg-OH peak increases significantly, while the Mg-O peak decreases, which proves that the formed Mg-FOH is the main adsorption mechanism, and Mg-F is auxiliary adsorption mechanism. Figure 7.f shows La3d spectrum before and after 15LSMO adsorption. The main peaks of La3d5/2 and La3d3/2 before adsorption are located at 835.7eV and 852.5eV, respectively, and the corresponding satellite peaks are located at 839.0eV and 855.8eV, respectively. These peaks confirm the presence of La_2O_3. After adsorption, the binding energy of La3d5/2 and La3d3/2 becomes higher, which represents the formation of new lanthanum compounds (Wu et al. 2017).

3.2. Effect of La impregnation ratio

Fig.S1 shows the effect of different lanthanum impregnation ratios on the removal of fluoride from the material. In the range of impregnation ratio from 10–20%, the fluorine removal balance tends to be balanced, and the fluorine removal rate reaches more than 90%. Among them, the material with 15% impregnation ratio (15LSMO) has the largest fluorine removal rate, which is 93.1%. Therefore, 15LSMO is used as the analysis model in the experiment. The corresponding SEM images are shown in Fig.S2.

3.3 Kinetic and thermodynamic study

The Langmuir adsorption isotherm is assumed to be a homogeneous adsorption process, while the Freundlich adsorption isotherm is suitable for the equation of a heterogeneous system. As shown in Fig. 8, two models are used to fit the adsorption process of SMO and 15LSMO. The relevant parameters are shown in Table 2. The experimental results of the two materials are closer to the Langmuir adsorption isotherm, indicating that the adsorption on the surface of the adsorbent is homogeneous adsorption. However, theoretically, the maximum adsorption capacity of SMO is greater than 15LSMO, indicating that lanthanum-supported materials are more advantageous for low-concentration fluorine removal.

In order to further study the changes of the adsorption capacity of the two materials with time, the pseudo-first-order kinetic equation and the pseudo-second-order kinetic equation were used for kinetic simulation. The experimental diagram of the fitted adsorption kinetics is shown in Fig. 9. Table 3 is the

relevant data of the fitting results of the kinetic model. The correlation coefficient of the pseudo-second-order model of the two materials is higher, and the adsorption capacity value calculated by the pseudo-second-order kinetic model is closer to the actual value, which means that the fluorine removal mechanism on the surface of the material is mainly chemical adsorption.

3.4 Effect of pH and interfering anions

To investigate the effect of pH on the adsorption performance of the material, set the pH value from 2 to 12, a constant adsorbent dosage of 1g/L, an initial fluorine concentration of 10mg/L, and a contact time of 180min. The results are shown in Fig. 10. The results show that under acidic conditions, the material exhibits extremely high stability. Under alkaline conditions, even if the presence of OH- competes with F^- for OH^- active sites, However, the material has a significant effect on fluorine removal, when pH is 12. The fluorine removal performance does not change much in the pH range of 2–11. According to the comparison of the results of SMO and 15LSMO, it is speculated that the acid and alkali resistance of the material is derived from the presence of magnesium oxide.

To investigate the influence of interference ions on the adsorption performance of the material, set a constant adsorbent dosage of 1g/L, initial fluorine concentration of 10mg/L, interference ion concentration of 100mg/L, and contact time of 180min. The results are shown in Fig. 11. The results show that the interference ion has little effect on the fluorine removal efficiency of the material (< 4%).

4. Conclusion

In this paper, magnesia precursor powder is calcined to generate SMO, and then LSMO is prepared by impregnation method. According to the fluorine removal experiment research, it is found that 15LSMO has better fluorine removal efficiency, and then a series of characterization analysis comparisons are carried out through SMO and 15LSMO. BET results show that 15LSMO has a larger specific surface area and average pore size than SMO. SEM results show that lanthanum is successfully supported on the surface of the material. FT-IR and XPS spectroscopy results show that the fluorine removal mechanism of SMO and 15LSMO is OH- substitution, metal chemical adsorption (M-F), electrostatic attraction and carbonate substitution. The kinetic fitting results show that the adsorption rates of SMO and 15LSMO are closer to chemical adsorption, and the adsorption isotherm fitting results show that the adsorption process of SMO and 15LSMO is closer to the homogeneous adsorption process. After pH fluctuation and interfering ion influence experiment, for the initial fluorine concentration of 10mg/L, the highest fluorine removal efficiency of SMO can reach 82.7%, and the lowest is 77.3%. The fluorine removal efficiency of 15LSMO can meet the fluorine removal efficiency of more than 90% when the pH is less than 11, and it can meet the international standard of 1mg/L. In summary, 15LSMO has improved fluorine removal capacity and efficiency compared with SMO, so 15LSMO is a potential candidate material for adsorbent.

Declarations

Ethics approval and consent to participate Not applicable.

Consent for publication Not applicable.

Availability of data and materials Not applicable.

Competing interests The authors declare that they have no competing interests.

Funding This work was supported by the National Nature Science Foundation of China (21978048)； Scientific Innovation Research Foundation of College Graduate in Jiangsu Province (KYCX21_0091)；The Fundamental Research Funds for the Central Universities (2242015k30001), a Project Funded by the Priority Academic Program Development of Jiangsu Higher Education Institutions (PAPD) (1107047002), Fund Project for Transformation of Scientific and Technological Achievements of Jiangsu Province of China (BA2019054).

Authors' contributions Qiang Zhang planed and carried out the experimental work. Qingzhao Yao monitored the progress of the experiment and reviewed the draft. Wanying Chen, Fanli Zhang and Yang Liu contributed to the analysed and interpretation of results. Yuming Zhou provided the financial support for the project leading to this publication.

References

1. Ayoob S, Gupta AK (2006) Fluoride in Drinking Water: A Review on the Status and Stress Effects. Crit Rev Environ Sci Technol 36(6):433–487. doi: 10.1080/10643380600678112
2. Benedetti S, Nilius N, Myrach P, Valenti I, Freund H-J, Valeri S (2011) Spontaneous Oxidation of Mg Atoms at Defect Sites in an MgO Surface. J Phys Chem C 115(9):3684–3687. doi: 10.1021/jp1100158
3. Borgohain X, Boruah A, Sarma GK, Rashid MH (2020) Rapid and extremely high adsorption performance of porous MgO nanostructures for fluoride removal from water. J Mol Liq 305:112799. doi: 10.1016/j.molliq.2020.112799
4. Cadaval TRS, Dotto GL, Pinto LAA (2015) Equilibrium Isotherms, Thermodynamics, and Kinetic Studies for the Adsorption of Food Azo Dyes onto Chitosan Films. Chem Eng Commun 202(10):1316–1323. doi: 10.1080/00986445.2014.934449
5. Chowdhury IH, Chowdhury AH, Bose P, Mandal S, Naskar MK (2016) Effect of anion type on the synthesis of mesoporous nanostructured MgO, and its excellent adsorption capacity for the removal of toxic heavy metal ions from water. RSC Adv 6(8):6038–6047. doi: 10.1039/C5RA16837F
6. Descostes M, Mercier F, Thromat N, Beaucaire C, Gautier-Soyer M (2000) Use of XPS in the determination of chemical environment and oxidation state of iron and sulfur samples: constitution of a data basis in binding energies for Fe and S reference compounds and applications to the evidence of surface species of an oxidized pyrite in a carbonate medium. Appl Surf Sci 165(4):288–302. doi: 10.1016/S0169-4332(00)00443-8

7. He J, Yang Y, Wu Z, Xie C, Zhang K, Kong L, Liu J (2020) Review of fluoride removal from water environment by adsorption. J Environ Chem Eng 8(6):104516. doi: 10.1016/j.jece.2020.104516
8. He Y, Zhang L, An X, Wan G, Zhu W, Luo Y (2019) Enhanced fluoride removal from water by rare earth (La and Ce) modified alumina: Adsorption isotherms, kinetics, thermodynamics and mechanism. Sci Total Environ 688:184–198. doi: 10.1016/j.scitotenv.2019.06.175
9. Ho Y (2000) The kinetics of sorption of divalent metal ions onto sphagnum moss peat. Water Res 34(3):735–742. doi: 10.1016/S0043-1354(99)00232-8
10. Jia Y, Luo T, Yu X-Y, Liu J-H, Huang X-J (2013) Surfactant-free preparation of nickel carbonate hydroxide in aqueous solution and its toxic ion-exchange properties. New J Chem 37(2):534–539. doi: 10.1039/c2nj40983f
11. Jin Z, Jia Y, Luo T, Kong L-T, Sun B, Shen W, Meng F-L, Liu J-H (2015) Efficient removal of fluoride by hierarchical MgO microspheres: Performance and mechanism study. Appl Surf Sci 357:1080–1088. doi: 10.1016/j.apsusc.2015.09.127
12. Khalil KD, Riyadh SM, Jaremko M, Farghaly TA, Hagar M (2021) Synthesis of Chitosan-La2O3 Nanocomposite and Its Utility as a Powerful Catalyst in the Synthesis of Pyridines and Pyrazoles. Molecules 26(12). doi: 10.3390/MOLECULES26123689
13. Kuang M, Shang Y, Yang G, Liu B, Yang B (2019) Facile synthesis of hollow mesoporous MgO spheres via spray-drying with improved adsorption capacity for Pb(II) and Cd(II). Environ Sci Pollut Res Int 26(18):18825–18833. doi: 10.1007/s11356-019-05277-w
14. Li L-X, Di Xu, Li X-Q, Liu W-C, Jia Y (2014) Excellent fluoride removal properties of porous hollow MgO microspheres. New J Chem 38(11):5445–5452. doi: 10.1039/C4NJ01361A
15. Li T, Xie D, He C, Xu X, Huang B, Nie R, Liu S, Duan Z, Liu W (2016) Simultaneous adsorption of fluoride and hexavalent chromium by synthetic mesoporous alumina: performance and interaction mechanism. RSC Adv 6(54):48610–48619. doi: 10.1039/C6RA04604E
16. Maliyekkal SM, Anshup, Antony KR, Pradeep T (2010) High yield combustion synthesis of nanomagnesia and its application for fluoride removal. Sci Total Environ 408(10):2273–2282. doi: 10.1016/j.scitotenv.2010.01.062
17. Maliyekkal SM, Sharma AK, Philip L (2006) Manganese-oxide-coated alumina: a promising sorbent for defluoridation of water. Water Res 40(19):3497–3506. doi: 10.1016/j.watres.2006.08.007
18. Newberg JT, Starr DE, Yamamoto S, Kaya S, Kendelewicz T, Mysak ER, Porsgaard S, Salmeron MB, Brown GE, Nilsson A, Bluhm H (2011) Formation of hydroxyl and water layers on MgO films studied with ambient pressure XPS. Surf Sci 605(1–2):89–94. doi: 10.1016/j.susc.2010.10.004
19. Niu H, Yang Q, Tang K, Xie Y (2006) Large-scale synthesis of single-crystalline MgO with bone-like nanostructures. J Nanopart Res 8(6):881–888. doi: 10.1007/s11051-006-9138-x
20. Nur T, Loganathan P, Nguyen TC, Vigneswaran S, Singh G, Kandasamy J (2014) Batch and column adsorption and desorption of fluoride using hydrous ferric oxide: Solution chemistry and modeling. Chem Eng J 247:93–102. doi: 10.1016/j.cej.2014.03.009

21. Sairam Sundaram C, Meenakshi S (2009) Fluoride sorption using organic-inorganic hybrid type ion exchangers. J Colloid Interface Sci 333(1):58–62. doi: 10.1016/j.jcis.2009.01.022
22. Shi Q, Huang Y, Jing C (2013) Synthesis, characterization and application of lanthanum-impregnated activated alumina for F removal. J Mater Chem A 1(41):12797. doi: 10.1039/c3ta12548c
23. Sing KSW (1985) Reporting physisorption data for gas/solid systems with special reference to the determination of surface area and porosity (Recommendations 1984). Pure Appl Chem 57(4):603–619. doi: 10.1351/pac198557040603
24. Sugama T, Sabatini R, Petrakis L (1998) Decomposition of Chrysotile Asbestos by Fluorosulfonic Acid. Ind Eng Chem Res 37(1):79–88. doi: 10.1021/ie9702744
25. Sun Y, Feng X, Zheng W (2020) Nanoscale Lanthanum Carbonate Hybridized with Polyacrylic Resin for Enhanced Phosphate Removal from Secondary Effluent. J Chem Eng Data 65(9):4512–4522. doi: 10.1021/acs.jced.0c00352
26. Sutradhar N, Sinhamahapatra A, Pahari SK, Pal P, Bajaj HC, Mukhopadhyay I, Panda AB (2011) Controlled Synthesis of Different Morphologies of MgO and Their Use as Solid Base Catalysts. J Phys Chem C 115(25):12308–12316. doi: 10.1021/jp2022314
27. Tan X, Fang M, Chen C, Yu S, Wang X (2008) Counterion effects of nickel and sodium dodecylbenzene sulfonate adsorption to multiwalled carbon nanotubes in aqueous solution. Carbon 46(13):1741–1750. doi: 10.1016/j.carbon.2008.07.023
28. Turner BD, Binning P, Stipp SLS (2005) Fluoride removal by calcite: evidence for fluorite precipitation and surface adsorption. Environ Sci Technol 39(24):9561–9568. doi: 10.1021/es0505090
29. Wang L, Xie Y, Yang J, Zhu X, Hu Q, Li X, Liu Z (2017) Insight into mechanisms of fluoride removal from contaminated groundwater using lanthanum-modified bone waste. RSC Adv 7(85):54291–54305. doi: 10.1039/C7RA10713G
30. Wu B, Fang L, Fortner JD, Guan X, Lo IMC (2017) Highly efficient and selective phosphate removal from wastewater by magnetically recoverable La(OH)3/Fe3O4 nanocomposites. Water Res 126:179–188. doi: 10.1016/j.watres.2017.09.034
31. Wuttke S, Coman SM, Scholz G, Kirmse H, Vimont A, Daturi M, Schroeder SLM, Kemnitz E (2008) Novel sol-gel synthesis of acidic MgF(2-x)(OH)(x) materials. Chemistry (Weinheim an der Bergstrasse. Germany) 14(36):11488–11499. doi: 10.1002/chem.200801702
32. Xu R, Zeng HC (2003) Dimensional Control of Cobalt-hydroxide-carbonate Nanorods and Their Thermal Conversion to One-Dimensional Arrays of Co 3 O 4 Nanoparticles. J Phys Chem B 107(46):12643–12649. doi: 10.1021/jp035751c
33. Yin L, Song S, Wang X, Niu F, Ma R, Yu S, Wen T, Chen Y, Hayat T, Alsaedi A, Wang X (2018) Rationally designed core-shell and yolk-shell magnetic titanate nanosheets for efficient U(VI) adsorption performance. Environmental pollution (Barking, Essex: 1987) 238:725–738. doi: 10.1016/j.envpol.2018.03.092
34. Zhang K, Wu S, Wang X, He J, Sun B, Jia Y, Luo T, Meng F, Jin Z, Lin D, Shen W, Kong L, Liu J (2015) Wide pH range for fluoride removal from water by MHS-MgO/MgCOâ‚ƒ adsorbent: kinetic,

thermodynamic and mechanism studies. J Colloid Interface Sci 446:194–202. doi: 10.1016/j.jcis.2015.01.049

35. Zhang Y, Jin Z, Min-He L, Guang-Song X, Min-Da X, Cheng H, Huang J (2021) Facile Synthesis of Hollow MgO Spheres and Their Fluoride Adsorption Properties. Adv Condens Matter Phys 2021(2):1–10. doi: 10.1155/2021/6655593
36. Zhang Y, Lin X, Zhou Q, Luo X (2016) Fluoride adsorption from aqueous solution by magnetic core-shell Fe3O4@alginate-La particles fabricated via electro-coextrusion. Appl Surf Sci 389(9):34–45. doi: 10.1016/j.apsusc.2016.07.087
37. Zur Theorie der sogenannten Adsorption gelöster Stoffe.Zeitschr f Chem und Ind der Kolloide2(1):15. doi: 10.1007/BF01501332

Tables

Table1 BET data of the prepared samples.

Sample	Specific surface area ($m^2 \cdot g^{-1}$)	Pore diameter (nm)	Pore volume ($cm^3 \cdot g^{-1}$)
SMO	216.76	4.04	0.23
15LSMO	232.41	17.05	0.66

Table 2 Langmuir and Freundlich adsorption isotherm parameters for fluoride on SMO and 15LSMO.

	Langmuir model			Freundlich model		
Equations	$q_e = \frac{q_m K_L C_e}{1 + K_L C_e}$			$q_e = K_F C_e^{\frac{1}{n}}$		
Parameter	q_m (mg/g)	K_L (L/mg)	R^2	K_F (mg/g)	n	R^2
SMO	171.368	0.0666	0.977	18.581	2.012	0.901
15LSMO	168.689	0.0939	0.977	22.836	2.128	0.917

Table 3 Kinetic parameters for fluoride adsorption on SMO and 15LSMO.

	Pseudo-first-order kinetic model			Pseudo-second-order kinetic model		
Equations	$q_t = q_e^{(1-e^{-K_1 t})}$			$q_t = \frac{K_2 q_e^{\ 2} t}{1 + K_2 q_e t}$		
Parameter	K_1 (1/min)	q_e (mg/g)	R^2	K_2 (g/(mg·min))	q_e (mg/g)	R^2
SMO	0.215	7.71	0.941	0.029	8.28	0.998
15LSMO	0.51	8.93	0.975	0.107	9.21	0.999

Figures

Figure 1

The XRD patterns of SMO and 15LSMO (LSMO at 15% lanthanum mass impregnation ratio).

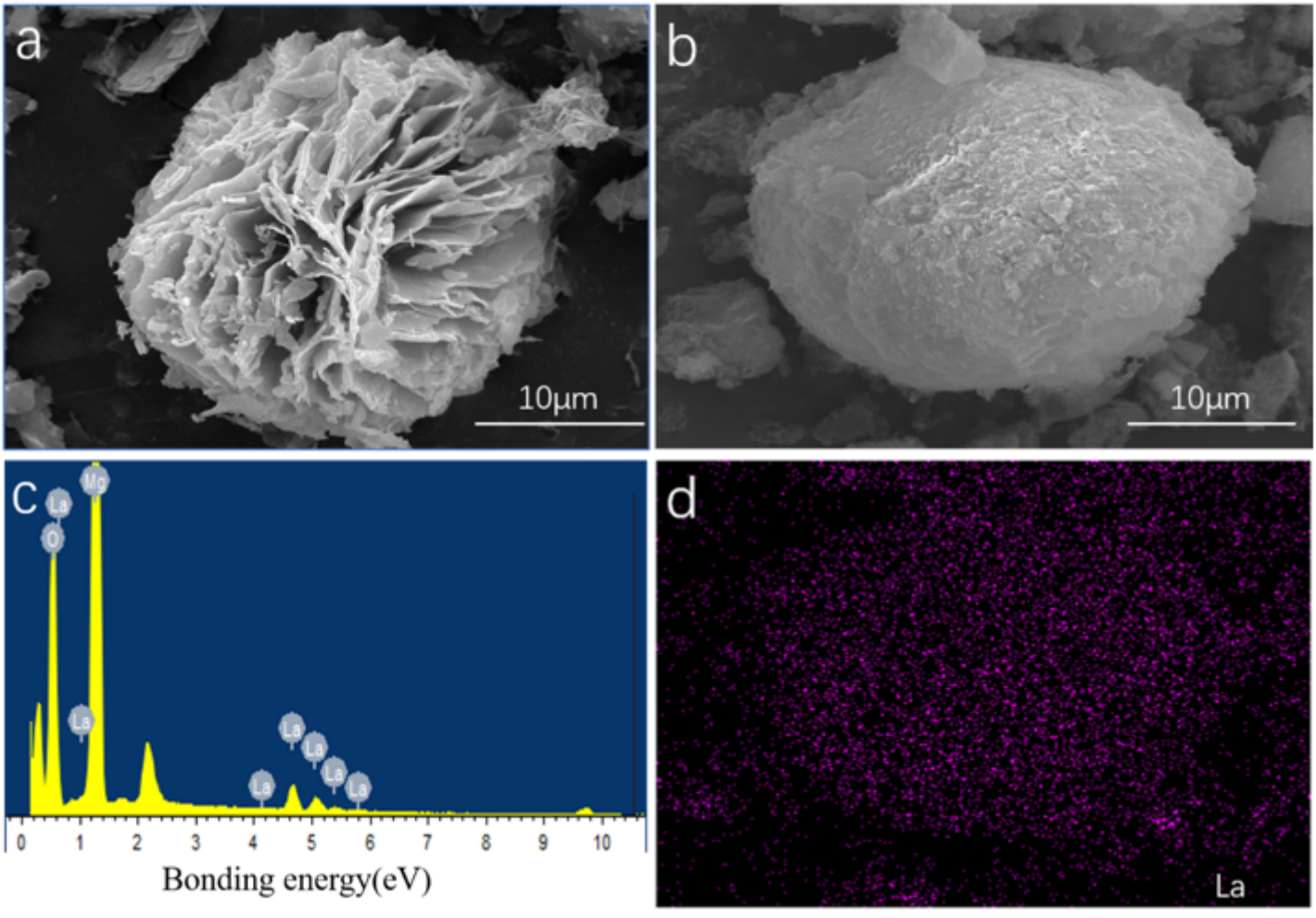

Figure 2

(a, b) The SEM images for SMO and 15LSMO; (c, d) The EDS spectrum and Scanning image of lanthanum distribution for 15LSMO.

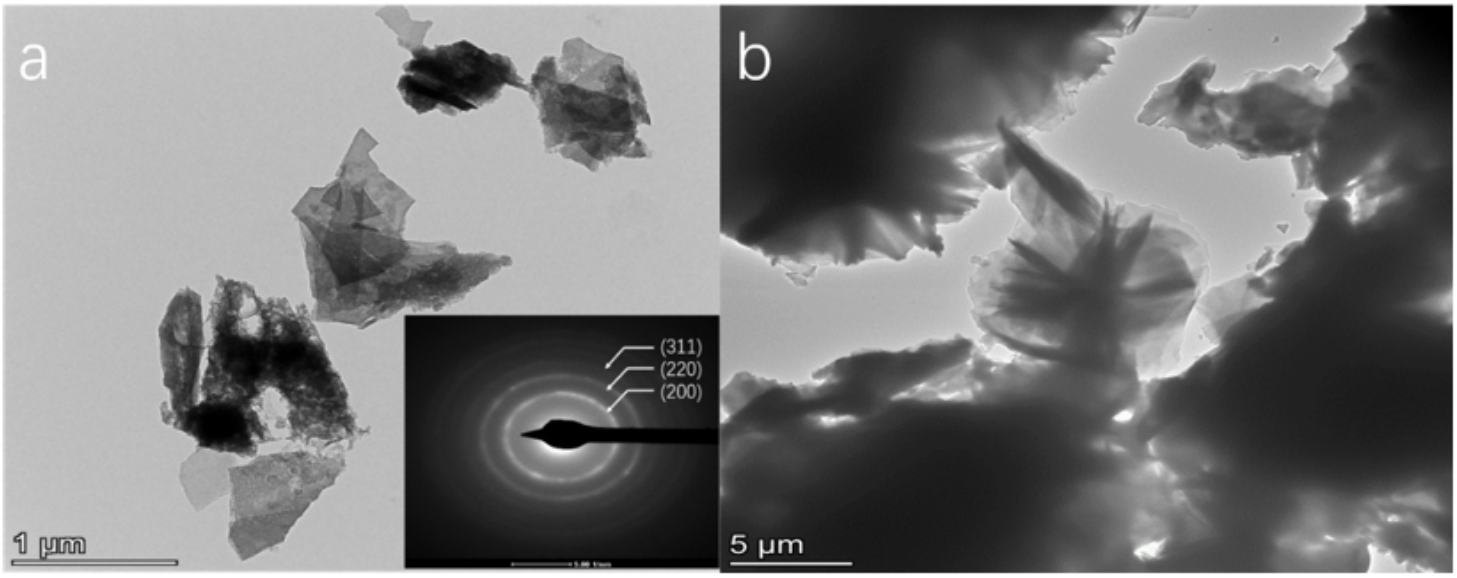

Figure 3

(a) The TEM image of scattered sheets of magnesium oxide and inside in (a) shows the corresponding SAED pattern;(b) The TEM image of edge of spheroidal magnesium oxide.

Figure 4

(a, b) N_2 adsorption-desorption isotherm and the corresponding pore size distribution of the SMO; (c, d) N_2 adsorption-desorption isotherm and the corresponding pore size distribution of the 15LSMO.

Figure 5

The FTIR spectra of SMO(a) and 15LSMO(b) before and after fluoride removal.

Figure 6

(a) XPS survey spectra of SMO before and after fluoride removal. (b-e) C1s O1s F1s and Mg2p spectra of SMO before and after fluoride adsorption.

Figure 7

(a) XPS survey spectra of 15LSMO before and after fluoride removal. (b-f) C1s O1s F1s Mg2p and La3d spectra of 15LSMO before and after fluoride adsorption

Figure 8

The plots of Langmuir, Freundlich isotherm model for F^- adsorption over (a)SMO, (b)15LSMO under different concentration of F^- (C_0=1-200mg/L, pH=7.0, dosage 1g/L).

Figure 9

The plots of pseudo-first-order, pseudo-second-order kinetic model for F^- adsorption over (a)SMO, (b)15LSMO (C_0 = 10mg/L, pH = 7.0, dosage = 1g/L).

Figure 10

Effect of initial pH on fluoride adsorption capacity of SMO and 15LSMO (dosage=1g/L, C_0=10mg/L, contact time=180min).

Figure 11

Effect of co-existing anions on fluoride adsorption capacity of SMO and 15LSMO (dosage=1g/L, C_0=10mg/L, contact time = 180min, co-existing anions concentration = 100mg/L).

Supplementary Files

This is a list of supplementary files associated with this preprint. Click to download.

- Supplementaryinformation.docx